Available online at www.sciencedirect.com
ScienceDirect
International Journal of Thermal Sciences 46 (2007) 561–572
International Journal of Thermal Sciences
www.elsevier.com/locate/ijts

Three-dimensional modelling of melt flow and segregation during Czochralski growth of Ge_xSi_{1-x} single crystals

S. Abbasoglu *, I. Sezai

Mechanical Engineering Department, Eastern Mediterranean University, Magosa, Mersin 10, Turkey

Received 24 November 2005; received in revised form 10 July 2006; accepted 10 July 2006

Available online 22 August 2006

Abstract

A series of unsteady three-dimensional (3-D) numerical simulations were carried out to examine the flow field and the radial segregation of silicon (Si) in a Ge_xSi_{1-x} melt during Czochralski (Cz) process. In addition to the gravity driven natural convection (buoyant convection), the effect of convection driven by surface tension on the free surface of the melt was included in the model, by considering thermal, as well as solutal Marangoni convection. The concentration and flow fields during crystal growth are presented for several temperature differences (ΔT), driving buoyant and Marangoni convection. It was found that the maximum silicon concentration difference at the growth interface decreases as temperature difference increases due to higher flow velocities in the vicinity of the interface. However, temporal fluctuations of Si concentration at the interface increase at higher temperature differences. The effects of aspect ratio (A_r) were also considered in the model. It was found that the radial segregation of Si at the crystal-melt interface improves as the aspect ratio of the melt in the crucible decreases.

Keywords: Czochralski; Ge_xSi_{1-x}; Marangoni convection; Segregation; Surface tension

1. Introduction

The alloys of Si and germanium (Ge) have a wide range of applications in microelectronic and optoelectronic devices such as optical switches, photo-detectors, solar cells, and power generators. In all these applications, the compositional uniformity of grown crystals is important. However, there are some difficulties during Ge_xSi_{1-x} growth with uniform composition because of the large differences in the properties of the constituent elements, such as the density and melting temperature. During the growth of the crystals, convection, resulting from buoyancy and surface tension forces in the melt, is often oscillatory or even turbulent in large systems and these unsteady melt motions lead to fluctuations. If $k_s > 1$, where the segregation coefficient k_s is the ratio of the local dopant concentration in the crystal to that in the melt at any point along the crystal-melt interface, dopants are preferentially absorbed into the crystal. These fluctuations break the balance of dopant distribution between the absorption rate and the rate of diffusion through the crystal in the growth interface and cause variations in the crystal's dopant composition. Fluctuations in the melt velocity also lead to striations as they convect dopant in and out of species-diffusion boundary layer or radially within the layer. Also, 3-D flow in the melt generates a non-uniform solute concentration distribution along the growth interface, which also affects the quality of the grown crystal. In addition, convection driven by the surface tension may lead to unsteady flows and temperature variations in the melt. It may also induce undesirable variations in the growth velocity, and also a non-uniform solutal composition in the melt near the growth interface. These variations incorporate micro-segregations, the growth striations, into the grown crystal. Therefore, a large number of studies were conducted in order to understand the effect of Marangoni convection in Cz growth method [1–7]. The results show that even in low-*Pr* melts, the presence of Marangoni convection strongly affects the flow pattern and so ignoring Marangoni convection causes a large deviation of flow fields. It is also found that under the effect of Marangoni convection, the flow becomes quickly 3-D and oscillatory, which, in turn affects the transport of dopants.

* Corresponding author. Tel.: +90(392) 630 1355; fax: +90(392) 365.
E-mail address: serkan.abbasoglu@emu.edu.tr (S. Abbasoglu).

1290-0729/$ – see front matter
doi:10.1016/j.ijthermalsci.2006.07.010

Nomenclature

A_r	aspect ratio, H/r_{cru}
Bi_{rad}	Biot number for radiation heat transfer, $\frac{r_{\text{cru}}}{k}\varepsilon\sigma(T+T_a)(T^2+T_a^2)$
C	dimensionless molar fraction of Si, $(C^*-C_o^*)/\Delta C^*$
C_o^*	initial molar fraction of Si in the melt
C^*	molar fraction of Si in the melt
C_{ave}	average Si concentration at the growth interface
C_P	specific heat capacity ..... $\text{J kg}^{-1}\text{ K}^{-1}$
D	diffusion coefficient ..... $\text{m}^2\text{ s}^{-1}$
$dC_{\max}$	maximum Si concentration difference at the crystal-melt interface
ΔC^*	reference concentration difference, $C_o^*\lvert(1-k_s)\rvert\upsilon_L\frac{r_{\text{cru}}}{D}$
ΔT	reference temperature difference, T_h-T_m
g	gravitational acceleration ..... m s^{-2}
H	crucible height ..... m
k	thermal conductivity ..... $\text{W m}^{-1}\text{ K}^{-1}$
k_s	segregation coefficient
Ma_C	solutal Marangoni number, $-\partial\gamma/\partial C^*(\Delta C^* r_{\text{cru}}/\mu\alpha)$
Ma_T	thermal Marangoni number, $-\partial\gamma/\partial T(\Delta T r_{\text{cru}}/\mu\alpha)$
P	dimensionless pressure
Pr	Prandtl number, ν/α
R	dimensionless radial distance, r/r_{cru}
r	radial distance ..... m
R_{cry}	dimensionless crystal radius, $r_{\text{cry}}/r_{\text{cru}}$
Ra_C	solutal Rayleigh number, $g\beta_C\Delta C^* r_{\text{cru}}^3/\nu D$
Ra_T	thermal Rayleigh number, $g\beta_T\Delta T r_{\text{cru}}^3/\nu\alpha$
r_{cru}	crucible radius ..... m
Sc	Schmidt number, ν/D
T	temperature ..... K
t	dimensionless time
U	dimensionless radial velocity component
V	dimensionless circumferential velocity component
V_L	dimensionless crystal pulling rate
W	dimensionless vertical velocity component
$\partial\gamma/\partial T$	temperature coefficient of surface tension ..... $\text{N m}^{-1}\text{ K}^{-1}$
$\partial\gamma/\partial C^*$	concentration coefficient of surface tension ..... N m^{-1}/% Si
Z	dimensionless vertical distance, z/r_{cru}

Greek symbols

α	thermal diffusivity ..... $\text{m}^2\text{ s}^{-1}$
β_C	solutal expansion coefficient ..... 1/% Si
β_T	thermal expansion coefficient ..... K^{-1}
σ	Stefan–Boltzmann constant, $5.67040\times10^{-8}\text{ W m}^{-2}\text{ K}^{-4}$
Θ	dimensionless temperature, $(T-T_m)/\Delta T$
Θ_a	dimensionless ambient temperature, $(T_a-T_m)/\Delta T$
ε	emissivity
μ	dynamic viscosity ..... $\text{kg m}^{-1}\text{ s}^{-1}$
τ_p	period
ν	kinematic viscosity ..... $\text{m}^2\text{ s}^{-1}$
ρ	density ..... kg m^{-3}

Subscripts

a	ambient
C	solutal
cru	crucible
cry	crystal
h	heated wall
m	melting
T	thermal

There are also some studies to identify the segregation phenomena in Cz growth method. The experimental studies in Refs. [8–11] are mainly related with the solute segregation along the axial direction in the Cz growth of Ge_xSi_{1-x} bulk alloy crystals. The growth velocity, the distribution coefficient, the compositional variation along the pulling axis and the grown-in defects of the crystal are discussed in these studies. Segregation phenomena in the Cz growth of semiconductor compounds was studied numerically [12–14], demonstrating the strong effects of flow patterns and heat transfer on solute distribution. In the two-dimensional (2-D) model of Xiao [12], it was also found that due to the strong flow, the extra solute is transported away faster from the interface, which decreases the concentration level in the solid. A transient 2-D convection-diffusion model was developed by Wang et al. [13] to simulate the segregation phenomena in batchwise and continuous Cz process. It was observed that the dopant concentration in the melt and the maximum concentration difference at the crystal-melt interface increase gradually as the melt depth is decreased in the batchwise Cz process. A 2-D model for the unsteady transport of a dopant during the liquid encapsulated Cz growth process with a steady axial magnetic field was presented by Morton et al. [14] and the dopant distributions in the crystal and in the melt at several stages during growth are presented. It was found that the convective species transport during growth produces concentration differences in both the melt and the crystal. Enger et al. [15] compared measured and predicted temperature readings in an industrial Cz melt during real crystal growth conditions. The predictions were based on 3-D unsteady simulations of the flow and heat transfer. From experiments and numerical simulations it was shown that a higher crucible rotation damps the temperature fluctuations under the crystal. Turbulent 2-D and 3-D models were used for the entire Cz system by Smirnova et al. [16] to study the heat transfer and melt flow in the growth of Ge_xSi_{1-x} crystals, but species transport in the melt was neglected. The computations showed that melt convection is an important aspect of the Ge_xSi_{1-x} Cz growth, and it is necessary to account for accurate prediction of the process.

In the growth of Ge_xSi_{1-x} alloys, besides buoyant and thermal Marangoni convections, the solutal Marangoni convection

may affect the solute distribution in the melt. As a result, in addition to buoyant and thermal Marangoni convections, solutal Marangoni convection should be included in predicting the dopant distribution in the Cz growth of semiconductor materials. To the knowledge of the present authors there is no 3-D study incorporating species transport and solutal Marangoni convection during the growth of semiconductor materials. The present study examines the role of the buoyant and Marangoni convections in the melt on the radial segregation of Si at the growth interface during the growth process of Ge_xSi_{1-x} ($x = 0.95$, 5% Si) with Cz configuration. For this purpose a transient 3-D model is developed and the effect of buoyant and Marangoni convections on the flow and concentration fields were elucidated. In addition, the effect of different aspect ratios was investigated.

2. Numerical model

Fig. 1 shows the schematic diagram used to model the configuration of the idealized system. For simplicity, the free surface and the crystal-melt interface are assumed to be flat. The temperature of the crystal-melt interface is assumed to be at the melting point T_m, and the side wall to be at a higher temperature T_h. The bottom surface is assumed to be adiabatic. Heat loss from the free surface of the melt is assumed to be due to radiation alone to an ambient temperature T_a. The crucible and the crystal are stationary. The flow is assumed to be incompressible and the fluid is Newtonian. Owing to the Boussinesq approximation, the melt density is only considered in the calculation of the body forces induced by thermal and solutal buoyancy. Other fluid properties are assumed to be constant and the surface tension γ changes linearly with temperature and concentration. The following governing equations were written in non-dimensional forms by using r_{cru}, ν/r_{cru}, r_{cru}^2/ν and $\rho\nu^2/r_{\text{cru}}^2$ respectively, as the scale factors for the length, velocity, time and pressure so that all important quantities can be taken into account without loss of accuracy. In addition, the non-dimensional temperature and concentration are defined as $\Theta = (T - T_m)/(\Delta T)$ and $C = (C^* - C_o^*)/\Delta C^*$, respectively.

$$\nabla \cdot \mathbf{V} = 0 \tag{1}$$

$$\frac{\partial \mathbf{V}}{\partial t} + (\mathbf{V}\cdot\nabla)\mathbf{V} = -\nabla P + \nabla^2\mathbf{V} + \frac{Ra_T}{Pr}\Theta + \frac{Ra_C}{Sc}C \tag{2}$$

$$\frac{\partial \Theta}{\partial t} + \mathbf{V}\cdot\nabla\Theta = \frac{1}{Pr}\nabla^2\Theta \tag{3}$$

$$\frac{\partial C}{\partial t} + \mathbf{V}\cdot\nabla C = \frac{1}{Sc}\nabla^2 C \tag{4}$$

where $\mathbf{V} = (U, V, W)$.

The applied boundary conditions are:

Along the bottom wall ($Z = 0$, $0 < R < 1$);

$$U = V = W = 0, \qquad \frac{\partial\Theta}{\partial Z} = 0, \qquad \frac{\partial C}{\partial Z} = 0 \tag{5}$$

Along the crystal-melt interface ($Z = A_r$; $0 < R < R_{\text{cry}}$);

$$U = V = W = \Theta = 0$$
$$\frac{\partial C}{\partial Z} = C(1-k_s)V_L Sc + 1 \tag{6}$$

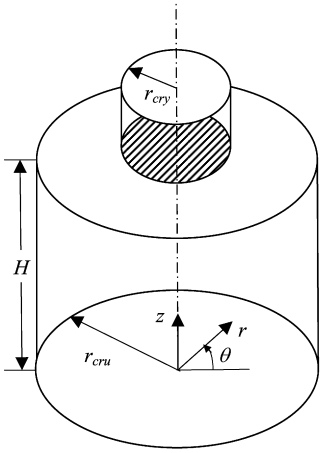

Fig. 1. Schematic configuration of the Cz model.

Along the free surface ($Z = A_r$; $R_{\text{cry}} < R < 1$);

$$\frac{\partial U}{\partial Z} = -\frac{Ma_T}{Pr}\frac{\partial\Theta}{\partial R} - \frac{Ma_C}{Pr}\frac{\partial C}{\partial R}$$
$$\frac{\partial V}{\partial Z} = -\frac{1}{R}\frac{Ma_T}{Pr}\frac{\partial\Theta}{\partial\theta} - \frac{1}{R}\frac{Ma_C}{Pr}\frac{\partial C}{\partial\theta} \tag{7}$$
$$W = 0, \qquad \frac{\partial\Theta}{\partial Z} = -Bi_{\text{rad}}(\Theta - \Theta_a), \qquad \frac{\partial C}{\partial Z} = 0$$

Along the side walls ($0 < Z < A_r$; $R = 1$);

$$U = V = W = 0, \qquad \Theta = 1, \qquad \frac{\partial C}{\partial Z} = 0 \tag{8}$$

The governing equations and the boundary conditions are discretized by using the finite volume method in staggered, non-uniform grids. SIMPLEC algorithm [17] is used to couple the momentum and continuity equations. QUICK scheme [18] is used in approximating the advection terms on control volume faces. The momentum equations are solved by applying one iteration of the strongly implicit procedure (SIP) [19] which is extended here to handle 3-D problems. The pressure correction equations are solved iteratively by applying the conjugate gradient (CG) method [20]. The energy and species concentration equations are solved iteratively by using the Bi-CGSTAB method [21]. Calculations presented in this article were performed using non-uniform grids, which are constructed with finer meshes in the regions under the free surface and near the bottom and sidewalls where boundary layers develop. The circumferential direction has uniform grids in all cases. In order to examine the grid dependence, numerical simulations with three different meshes, i.e., $30^r \times 30^z \times 30^\theta$, $50^r \times 50^z \times 50^\theta$, $80^r \times 80^z \times 80^\theta$ are performed for the case of $Ma_T = 375$ and $Ra_T = 0$ with Cz configuration. The maximum difference in radial velocity, temperature and concentration at the free surface at $\theta = 0$ between $30^r \times 30^z \times 30^\theta$ and $50^r \times 50^z \times 50^\theta$ meshes are found to be about 8%, 3% and 1%, respectively while the difference is less than 1.8% in all variables listed above between $50^r \times 50^z \times 50^\theta$ and $80^r \times 80^z \times 80^\theta$ grids. Similar results were obtained for the variation of axial velocity at $R = 0.75$ and $\theta = 0$. Therefore, $50^r \times 50^z \times 50^\theta$ grids are chosen for the simulations in this study. The time stepping has been realized

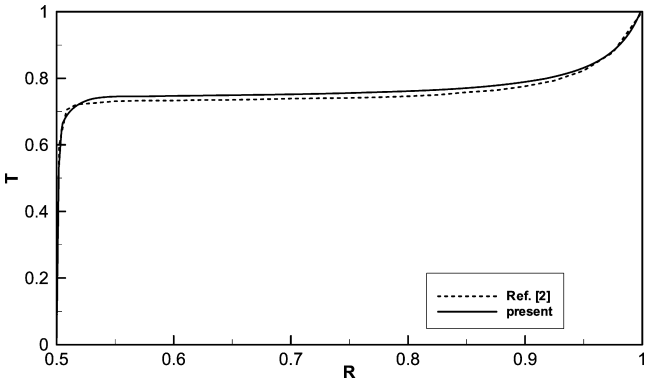

Fig. 2. Radial distribution of temperature on the liquid surface with $Pr = 6.7$, $Ma_T = 3.34 \times 10^4$ and $A_r = 0.275$ in an annular pool.

with the second order, fully implicit, backward Euler scheme. The time step is taken as 5×10^{-5}. The present numerical code is validated by comparing the temperature distribution at the liquid surface with the numerical results of Li et al. [2] for the case of $Ma_T = 3.34 \times 10^4$ and $Ra_T = 0$ with $Pr = 6.7$ in an annular pool. The inner and outer cylinders are maintained at constant temperatures, where the outer cylinder is assumed as hot and the inner cylinder is cold. At the top free surface, the thermocapillary force is taken into account. At other solid–liquid boundaries, the no-slip condition is applied. Both bottom and top boundaries are assumed to be adiabatic. The results obtained are in good agreement as shown in Fig. 2. The CPU time required for each simulation was approximately 10 days on a 3.00 GHz Pentium IV personal computer with 2 GB RAM. The difficulty in solving for the velocity components at the centre of the cylinder is circumvented by using the technique proposed by Ozoe and Toh [22].

3. Results and discussion

The thermophysical properties of Ge_xSi_{1-x} alloy and the parameters used in the simulations are provided in Table 1 where the properties are taken from references [23–27]. The calculations in this section are performed for a crucible of aspect ratio $A_r = 1$ and a crucible radius of 10 mm. The crystal pulling rate, υ_L, is set to 2 mm/h in accordance with the pulling rate used in the growth experiments in reference [9], where a small scale crucible is used for the growth of Ge_xSi_{1-x}. Since the change in the concentration of Si during the simulation period is small, constant values of $k_s = 4.2$ and $T_m = 1271.3$ K are used, which correspond to Si concentration of 5%, in accordance with the phase diagram of $Ge_{1-x}Si_x$ [28] and reference [25], respectively. For studies involving larger concentration differences at the crystal-melt interface the effect of Si concentration on melting temperature and on segregation coefficient should be taken into consideration. The total growth times simulated in the paper corresponds to a melt volume change of less than 0.5%. Crystal height which is grown is only 0.05 mm. As a result the change in the melt volume is not taken into account during a simulation period. The solutal Rayleigh number and solutal Marangoni number are set to $Ra_C = 3 \times 10^6$ and $Ma_C = 120$, respectively, in accordance with the initial 5% Si concentration in the melt. The results of the steady state simulation for $\Delta T = 1.0$ K, which corresponds to $Ra_T = 385$ and $Ma_T = 50$ were used as initial conditions for temperature and velocities. For the initial Si concentration $C = 0$ is used in the melt at the start of the growth process. The simulations were carried out for different cases with different values of ΔT, which changes between 5 and 25 K. However, only three cases are examined here, starting with $\Delta T = 6.0$ K as it is slightly above the threshold value for the start of unsteady flow. All the parameters and values presented in the figures are dimensionless.

Table 1
Thermophysical properties of Ge_xSi_{1-x} and other parameters

Property	Symbol	Value	Unit
Ambient temperature	T_a	1241.3	K
Concentration dependence of surface tension coefficient	$\partial\gamma/\partial C^*$	2.2×10^{-3}	$kg\,s^{-2}$
Density	ρ	5246	$kg\,m^{-3}$
Diffusion coefficient	D	1.0×10^{-8}	$m^2\,s^{-1}$
Dynamic viscosity	μ	7.35×10^{-4}	$kg\,m^{-1}\,s^{-1}$
Emissivity	ε	0.3	–
Initial molar fraction of Si	C_o^*	0.05	–
Gravitational acceleration	g	9.81	$m\,s^{-2}$
Kinematic viscosity	ν	1.4×10^{-7}	$m^2\,s^{-1}$
Melting temperature	T_m	1271.3	K
Prandtl number	Pr	6.37×10^{-3}	–
Schmidt number	Sc	14	–
Segregation coefficient	k_s	4.2	–
Specific heat capacity	C_P	443	$J\,kg^{-1}\,K^{-1}$
Solutal expansion coefficient	β_C	5.0×10^{-3}	1/ at % Si
Temperature dependence of surface tension coefficient	$\partial\gamma/\partial T$	-8.1×10^{-5}	$kg\,s^{-2}\,K^{-1}$
Thermal conductivity	k	51.1	$W\,m^{-1}\,K^{-1}$
Thermal diffusivity	α	2.199×10^{-5}	$m^2\,s^{-1}$
Thermal expansion coefficient	β_T	1.2×10^{-4}	K^{-1}

Fig. 3 shows the transient response of the circumferential velocity component at the monitoring point, which is located at the free surface in the middle of the outer radius of the crystal and the crucible wall. The results are obtained for $\Delta T = 6.0, 12.5, 20.0$ K which corresponds to $Ra_T = 2300, 4780, 7650$ and $Ma_T = 300, 625, 1000$, respectively. The corresponding power spectra of the time varying component of the signal $(V - \overline{V})$, which is obtained by subtracting the time average value from instantaneous value, is depicted in Fig. 4. For small radial temperature differences the basic flow structure is steady and axisymmetric. However, when the temperature difference exceeds certain threshold value, the flow becomes unstable against 3-D disturbances and oscillations are set in the basic flow structure. The small scale oscillations observed in Fig. 3(a) indicates that $\Delta T = 6.0$ K is slightly above the threshold value for the start of unsteady flow. The oscillations begin at $t \approx 0.4$ for $\Delta T = 6.0$ K. The oscillations are periodic with a single frequency of 156.30. Starting from the same initial conditions oscillations begin earlier in time at the higher ΔT. Also, at higher ΔT values the amplitude of the oscillations increases. Similar observations were found in pure thermocapillary convection in open cylindrical annuli in the absence of gravity [29]. For $\Delta T = 12.5$ K low frequency oscillations are added to the periodic signal (Fig. 4(b)). The strong broadband noise in the

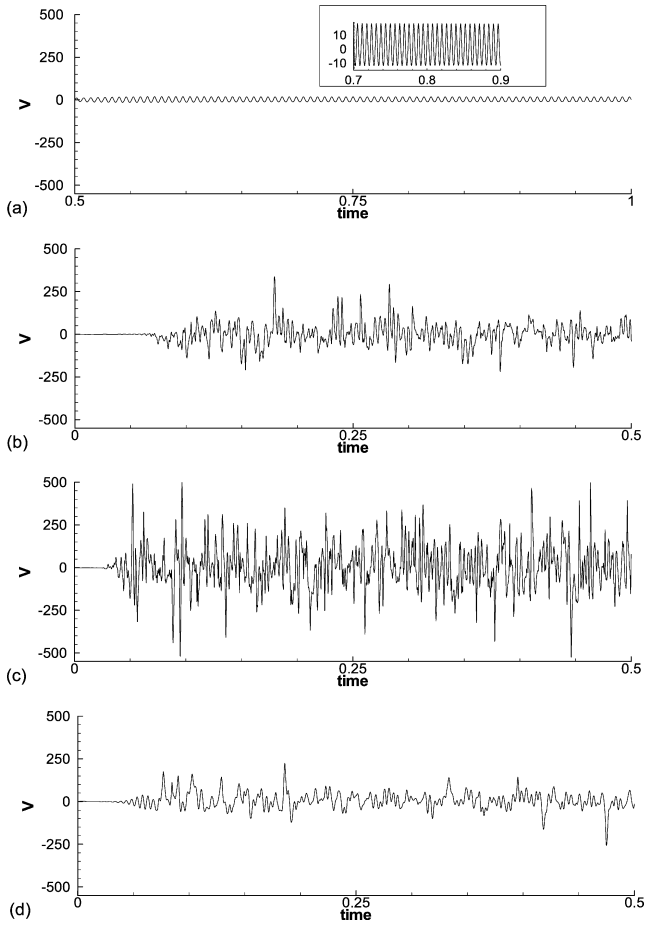

Fig. 3. The time dependency of the circumferential velocity components for three different temperature differences at the monitoring point, (a) $\Delta T = 6.0$ K, (b) $\Delta T = 12.5$ K, (c) $\Delta T = 20.0$ K, (d) $\Delta T = 20.0$ K and $Ma_T = Ma_C = 0$.

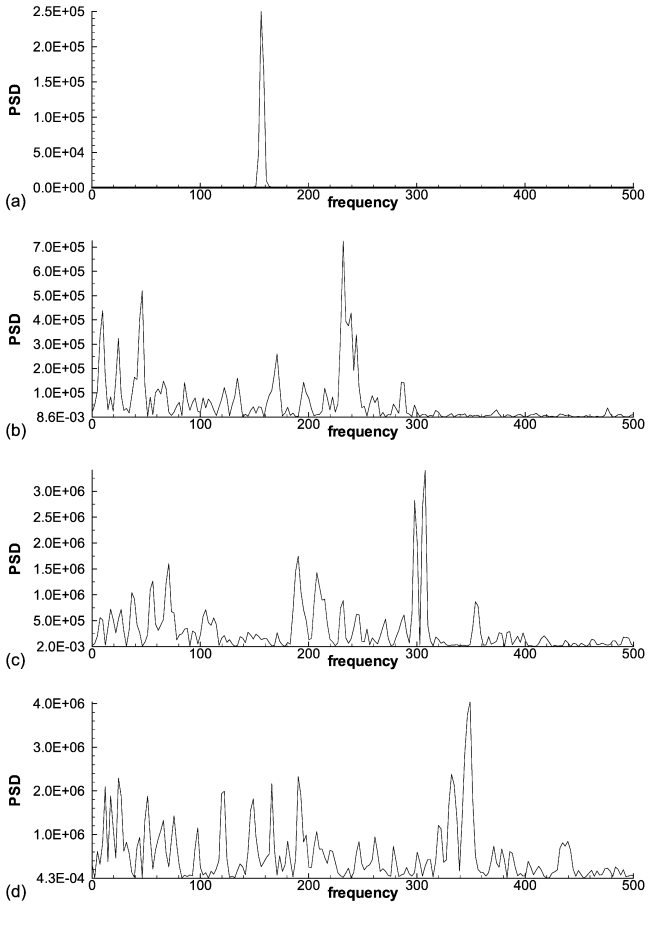

Fig. 4. Power spectral density of the circumferential velocity fluctuations for three different temperature differences, (a) $\Delta T = 6.0$ K, (b) $\Delta T = 12.5$ K, (c) $\Delta T = 20.0$ K, (d) $\Delta T = 20.0$ K and $Ma_T = Ma_C = 0$.

power spectrum observed for the case of $\Delta T = 20.0$ K suggests that the flow is in a chaotic regime at higher values (Figs. 4(c)). On the other hand, when Marangoni convection is neglected, as in Figs. 3(d) and 4(d), it is found that the amplitude of the oscillations at $\Delta T = 20.0$ K is even smaller than the oscillations at $\Delta T = 12.5$ K. Therefore, it can be concluded that the Marangoni convection increases flow intensity in the melt.

The flow fields are presented by the projection of the flow lines during four different instances of a period (τ_p) at $t = 0.80$ corresponding to the dominant frequency for $\Delta T = 6.0$ K in the vertical plane at $\theta = 0$ in Fig. 5. The projections of flow lines on vertical (R, Z)-plane are obtained from the in-plane components of the U and W velocity vectors on that plane. The high temperature at the side wall of the crucible initiates the buoyancy driven flow and there is a rising motion along the crucible wall due to the buoyancy effect. In addition, the thermocapillary force drives the melt flow from the crucible wall towards the crystal at the free surface. In the region underneath the crystal and away from the crystal-melt interface, a strong downward flow is observed in the core of the crucible. The central downward flow penetrates to the bottom wall and flows outward along the bottom wall, creating a toroidal cell. This main vortex occupies almost all the melt volume. It is observed that a small reverse vortex is developed at the side top wall of the crucible. This small vortex is a secondary vortex induced by the flow of the large toroidal cell. The vorticity of this secondary vortex is about 2% of the main toroidal vortex. There are also other weak vortices, the vorticity of which is only about 2% of that of the main toroidal vortex also, nested in the bottom corner near the crucible wall and under the crystal-melt interface. Similar to the flow fields reported in reference [30], all of these features of the flow field are almost in axisymmetry, as observed in Fig. 5. However, for higher ΔT values the axisymmetry is broken down and weak vortices under the crystal-melt interface disappear due to stronger Marangoni convection.

Projection of flow lines for $\Delta T = 6.0$ K on a horizontal plane close to the crystal-melt interface, $Z = 0.98$, clearly shows the formation of vortices under the crystal, in Fig. 6. The cross-section shown corresponds to the area below the crystal, namely $0 < R < 0.5$. The development of the vortices under the crystal-melt interface is attributed to the pulsating type of flow fluctuations during a period. The melt under the crystal bulges out radially along, roughly, east-west and north-south directions, while being squeezed radially inward along lines in between these directions (Figs. 6(b), (c) and (d)) during part of the period. This motion is reversed, as shown in Fig. 6(a), forming a pulsating type of flow. The observed azimuthal position of this pulsating type of flow is preserved in the whole

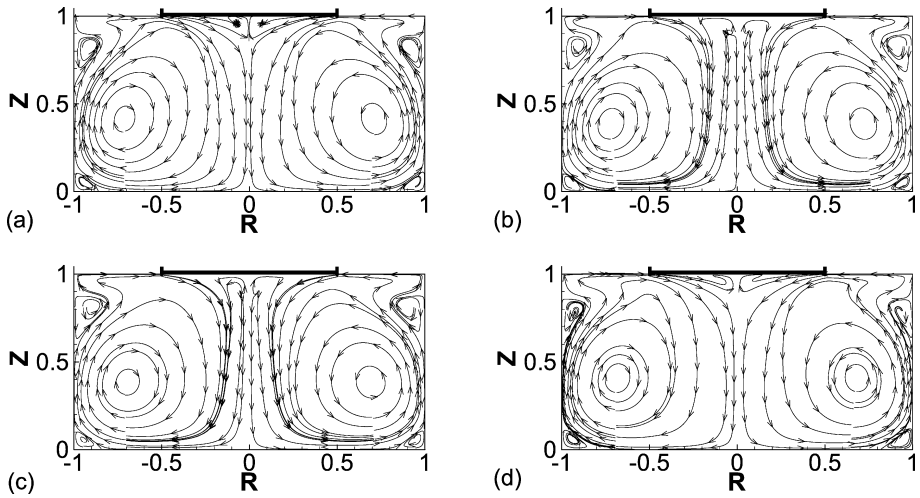

Fig. 5. The flow fields during four different instances of a period (τ_p) for $\Delta T = 6.0$ K in the vertical plane at $\theta = 0$, (a) t_o, (b) $t_o + 1/4\tau_p$, (c) $t_o + 1/2\tau_p$, (d) $t_o + 3/4\tau_p$, where $R_{\text{cry}} = R_{\text{cru}}/2$.

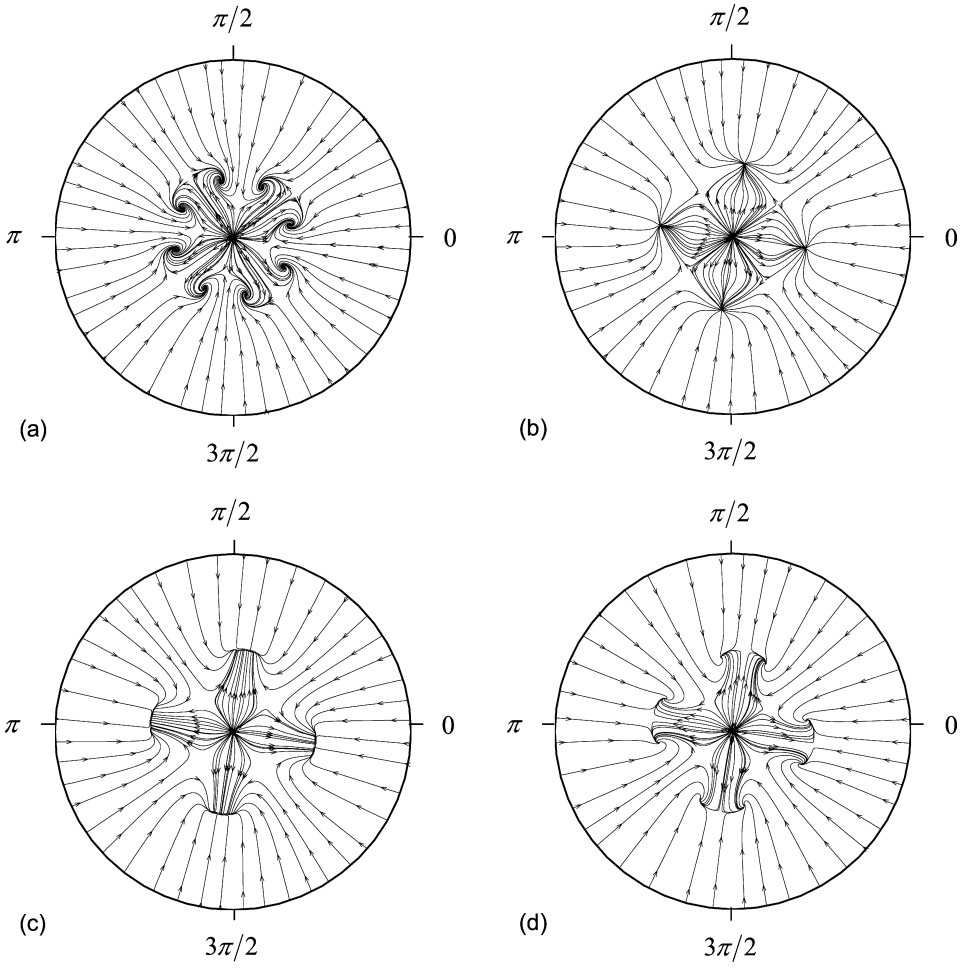

Fig. 6. Projection of flow lines on a horizontal plane at $Z = 0.98$ during four different instances of a period (τ_p) for $\Delta T = 6.0$ K, (a) t_o, (b) $t_o + 1/4\tau_p$, (c) $t_o + 1/2\tau_p$, (d) $t_o + 3/4\tau_p$.

periodic range up to $\Delta T = 10.0$ K, after which the fluctuations are no longer periodic. The invariant azimuthal position confirms the standing wave nature of the phenomenon which will be discussed later. The four pair of small vortices nested circumferentially at about $R \approx 0.25$ will affect the concentration profiles at the crystal-melt interface.

The iso-concentration lines during four different instances of a period at $t = 0.80$ are shown in Fig. 7 for periodic flow

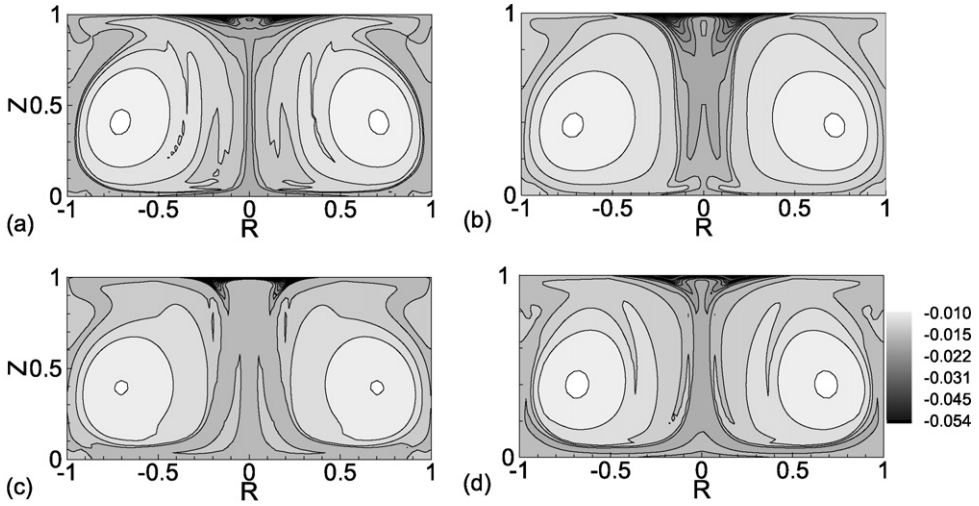

Fig. 7. The iso-concentration lines during four different instances of a period (τ_p) for $\Delta T = 6.0$ K in the vertical plane at $\theta = 0$, (a) t_o, (b) $t_o + 1/4\tau_p$, (c) $t_o + 1/2\tau_p$, (d) $t_o + 3/4\tau_p$.

regime for $\Delta T = 6.0$ K in the vertical plane at $\theta = 0$. Before solidification starts, the dopant concentration is uniform and this value is used to non-dimensionalize the concentration so that $C = 0$ everywhere in the melt at the beginning. Once crystal growth starts, a Si-low region is left near the crystal-melt interface as dopant (Si) is absorbed into the crystal since $k_s > 1$. The flow induced by the surface tension effect convects the melt with Si-low concentration away from the interface. The strong downward flow at the core of the melt near $R = 0$ produces a low Si concentration in this region. The closed constant concentration curves are in conformance with the toroidal flow structure shown earlier in Fig. 5 and produces rather uniform dopant region around the toroidal cell axis. On the other hand, Si concentration decreases sharply under the crystal-melt interface due to dopant absorption into the crystal. The oscillations of the two small weak vortices under the crystal-melt interface shown in Fig. 5 induce periodic variations in the concentration boundary layer near the central axis during an oscillation period (Fig. 7).

The iso-concentration lines at the plane of the growth interface are displayed in Fig. 8 during four different instances of a period starting from $t = 0.80$ for $\Delta T = 6.0$ K. The diameter displayed in the figure corresponds to that of the crystal. The radially inward flow at the surface carries the dopant rich melt towards the central axis at the crystal-melt interface. As the dopant is continuously absorbed by the crystal, its concentration decreases as the melt flows radially inward until it is opposed by the small vortical flow at about $R = 0.25$, which is flowing radially outward below the crystal, as shown in Fig. 5. In this region between, $R = 0.25$ and $R = 0.5$, the iso-concentration lines are concentric during a period indicating that Si concentration do not vary in the azimuthal direction during a period in this region. However, for $R < 0.25$ the Si concentration fluctuates during a period due to the pulsating type flow of the small vortices below the crystal. In this region there are 8 circumferentially aligned standing periodic rolls, which represent minimum values of the concentration of Si. As pointed out earlier during discussion of flow structure, in a region for which $R < 0.25$, the fluid under the crystal moves radially outward along approximately, the east-west and north-south directions, while it moves radially inward in between the indicated directions. This flow profile is reversed during the second half of a period, resulting in a pulsating type of flow structure. Each of the four pair of minimum concentration points are nested circumferentially along the bulge-out directions, which also change position during a period of oscillation.

Fig. 9 shows one cycle of the concentration oscillations at the crystal-melt interface along circumferential direction at $R = 0.10$. The waves are standing type pulsating waves.

The variation of the circumferentially and time-averaged Si concentration along the growth interface is shown in Fig. 10. The instantaneous velocity, temperature and concentration fields in the melt are highly random, and therefore it is difficult to predict any definite trend from this highly random distribution. Therefore, to filter out the fluctuations in the melt and to have an insight into the effect of the various ΔT, the concentration distribution in the r-direction at the free surface and crystal-melt interface was averaged by sampling the data during a period of fluctuations which was also averaged along the circumferential direction. During the simulations, the sampling started around $t = 0.80$ for $\Delta T = 6.0$ K and $t = 0.30$ for $\Delta T = 12.5$ and 20.0 K and continued through a period for each ΔT. It is found that Si concentration is uniform at the free surface; which is outside the domain shown in Fig. 8. This is attributed to the thermocapillary convection driven by the temperature difference at the free surface that prevents the development of the free surface concentration gradient. The upward moving fluid adjacent to the crucible's vertical wall carries the dopant-rich melt towards the free surface, where it is convected towards the crystal by the strong flow induced by the surface tension effect. As a result, the concentration is uniform and maximum at the free surface of the melt. The crystal is located in the region $-0.5 < R < 0.5$. The radially inward flow adjacent to the crystal-melt interface convects the dopant rich melt towards the radial centre. On this path the dopant is absorbed into the crystal as a result of which its concentration

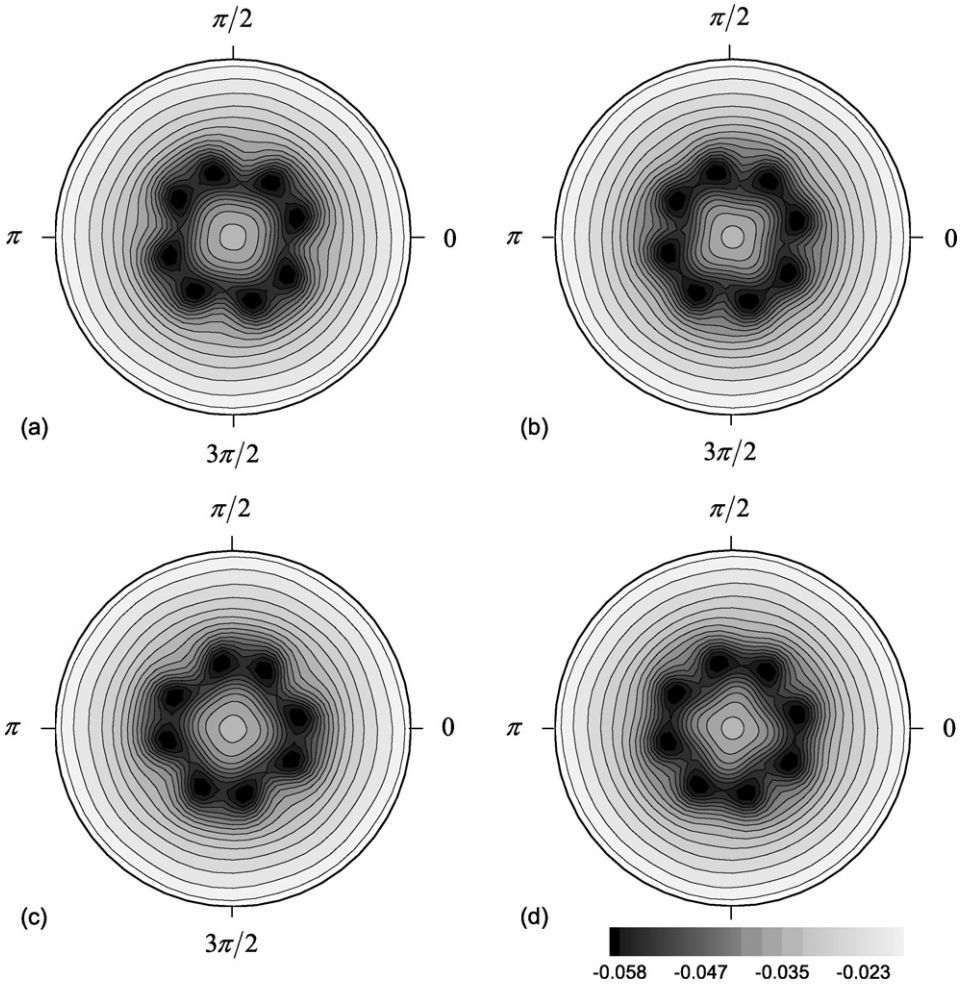

Fig. 8. Concentration distribution at the plane of the growth interface during four different instances of a period (τ_p) for $\Delta T = 6.0$ K, (a) t_o, (b) $t_o + 1/4\tau_p$, (c) $t_o + 1/2\tau_p$, (d) $t_o + 3/4\tau_p$.

decreases continuously. Similarly, the radially outward flow of the small vortices below the crystal-melt interface carries dopant-rich melt away from the centre during which its concentration decreases as a result of absorption into the crystal. The radially inward and outward flow adjacent to the crystal-melt interface meet at a point around $R = 0.25$, where Si concentration becomes minimum. At higher ΔT values the flow becomes stronger. As a result the Si in the high concentration melt has less time to be absorbed into the crystal during its journey below the crystal towards the minimum concentration point. Thus the difference between the maximum and minimum concentrations at the crystal-melt interface is smaller at higher ΔT values.

The time variation of the maximum Si concentration difference at the crystal-melt interface is displayed in Fig. 11 for different ΔT values during the growth process. Due to the reasons explained above the maximum concentration difference at the crystal-melt interface is smaller for higher ΔT flows. However, the amplitude of the maximum concentration difference increases at higher temperature differences. At $\Delta T = 6.0$ K the variation is periodic with rather low fluctuation amplitude. At higher ΔT values the maximum concentration difference at the crystal-melt interface is lower during the crystal growth period,

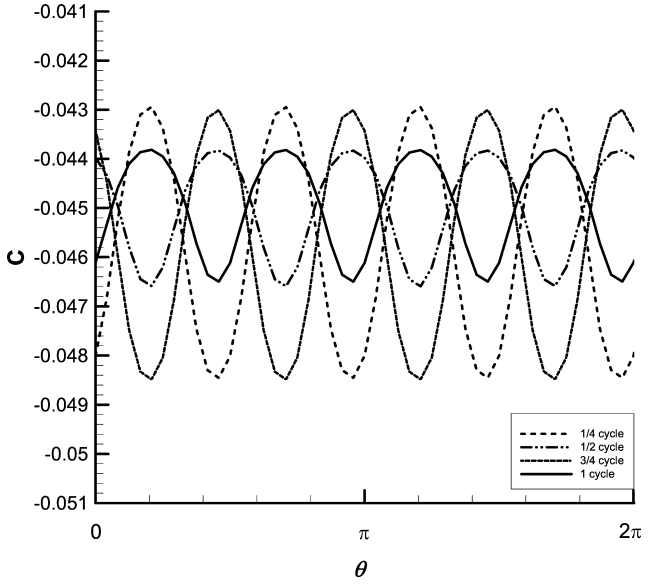

Fig. 9. One cycle of the concentration oscillations at the crystal-melt interface along circumferential direction at $R = 0.10$ for $\Delta T = 6.0$ K.

but the amplitudes of the fluctuations are higher exhibiting a chaotic behaviour, which may lead a non-axisymmetric dopant

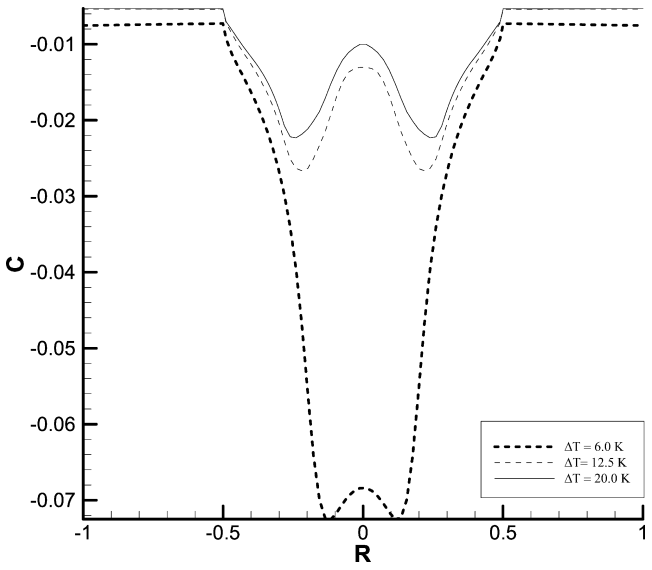

Fig. 10. Radial distribution of the circumferentially- and time-averaged Si concentration at the plane of the growth interface.

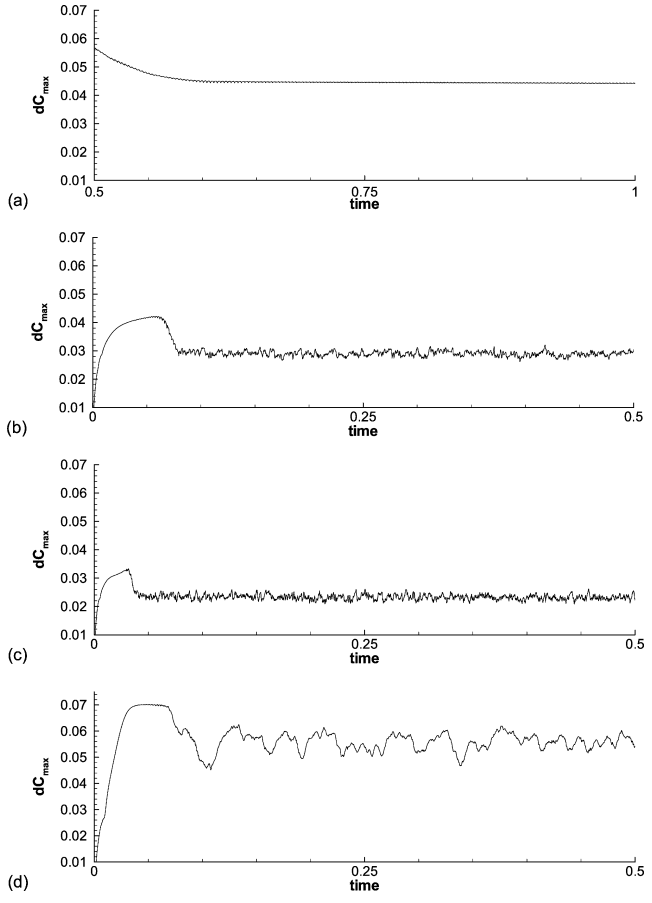

Fig. 11. The time variation of the maximum Si concentration difference at the growth interface for three different temperature differences, (a) $\Delta T = 6.0$ K, (b) $\Delta T = 12.5$ K, (c) $\Delta T = 20.0$ K, (d) $\Delta T = 20.0$ K and $Ma_T = Ma_C = 0$.

uniformity. Fig. 11(d) presents maximum Si concentration difference at the growth interface without Marangoni effect. It is observed that when Marangoni effect is neglected, maximum Si concentration difference is higher. This result can be attributed

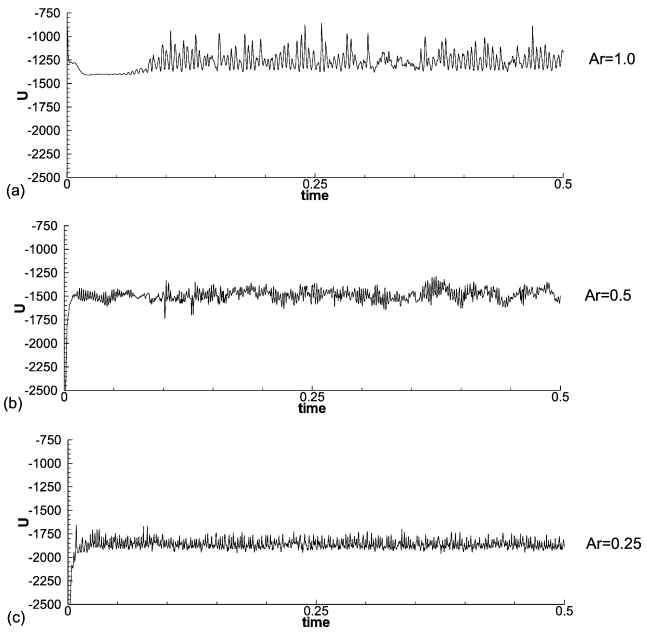

Fig. 12. The time dependency of radial velocity for different aspect ratios at the monitoring point for $\Delta T = 12.5$ K.

to the low flow intensity, which is mentioned in Figs. 3(d) and 4(d) that prevents better mixing in the melt.

In addition, during the growth process the amount of Si in the melt decreases due to the preferential absorption upon solidification since $k_s > 1$. As a result the average Si concentration at the growth interface decreases with time except during the initial stages where the average concentration increases for a short time interval after the initial sharp drop. The decrease in the average Si concentration at the growth interface will result in a gradual decrease in the Si content of the grown crystal along the growth direction as observed from the GeSi crystals grown on earth [7,8]. The variation of the average Si concentration at the growth interface involves small amplitude periodic oscillations at rather low values, ΔT values of 6.0 K. At higher temperature differences the amplitude of the average Si concentration at the interface is higher which will result in higher Si inhomogeneities in the grown crystal.

The above simulation results were presented for the melt in the Cz crucible with the aspect ratio of unity. However, during a batchwise Cz crystal growth process the height of the melt in the crucible and hence the aspect ratio of the melt decreases continuously. To find the effect of the change in the aspect ratio on the flow and dopant segregation, numerical simulations were repeated for two more aspect ratios of 0.5 and 0.25. However, in the simulations with $A_r = 0.5$ and 0.25, the same initial Si concentration (5%) is used although these cases corresponds to a later stage of the growth process where the Si concentration would be lower since Si in the melt is preferentially consumed at the crystal-melt interface.

Fig. 12 shows the time dependency of radial velocity component for three different aspect ratios at the monitoring point, which is located at the free surface at $R = 0.75$, for $\Delta T = 12.5$ K. The oscillations indicate that the flow is time-dependent and chaotic for all aspect ratios. However, the mag-

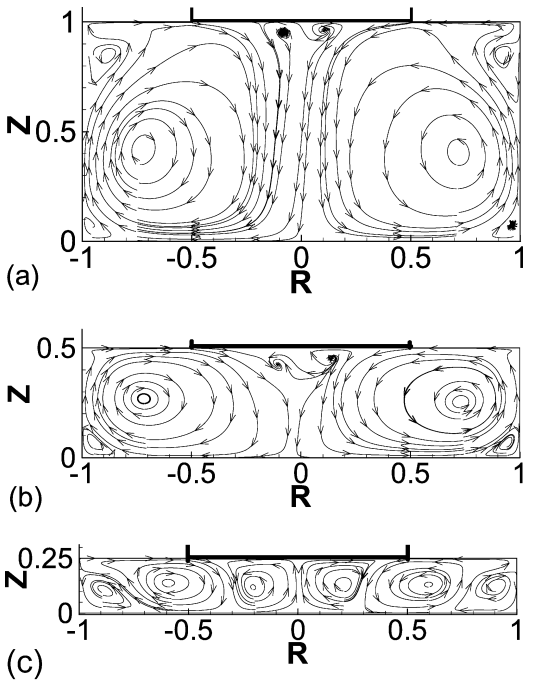

Fig. 13. The effect of aspect ratio of the melt on the time-averaged flow fields for $\Delta T = 12.5$ K, (a) $A_r = 1.0$, (b) $A_r = 0.5$, (c) $A_r = 0.25$.

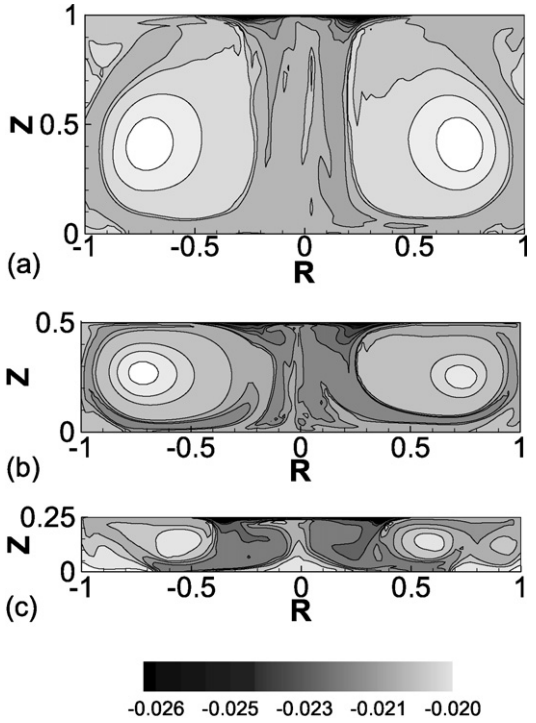

Fig. 14. The effect of aspect ratio of the melt on the time-averaged concentration fields for $\Delta T = 12.5$ K, (a) $A_r = 1.0$, (b) $A_r = 0.5$, (c) $A_r = 0.25$.

nitude of the velocities increases with decrease in A_r due to the relatively increased contribution of Marangoni convection.

Fig. 13 shows the effect of different aspect ratios on the flow fields for $\Delta T = 12.5$ K. The flow fields presented are time-averaged during the simulations, the sampling started around $t = 0.30$ and continued through a period for each case. For an aspect ratio of unity the flow is dominated with a toroidal roll cell with small vortices nested under the crystal-melt interface and in the bottom and top corner near the crucible. As the aspect ratio of the crucible is decreased, the flow adjusts itself to the new geometry by elongating the rolls. At $A_r = 0.5$ the two-roll flow structure of the melt in the crucible is still preserved. However, when the width/height ratio of the rolls reaches a critical limit the flow undergoes a bifurcation by forming new rolls, as a result of which the width/height ratio of the new rolls becomes smaller. This is similar to the formation of new rolls in Rayleigh–Benard convection in enclosures when the aspect ratio is reduced [31]. For $A_r = 0.25$ the flow structure in the melt consists of 6 rolls, where each pair of cells rotate in reverse direction. The two smaller rolls below the crystal are driven by the frictional effects of the surrounding larger rolls below the free surface. The increase in the number of rolls with decreasing A_r also occurs in thermocapillary convection in open cylindrical annuli heated from the outer wall [29] and in rectangular cavities [32].

Fig. 14 shows the effect of different aspect ratios on the time-averaged concentration fields for $\Delta T = 12.5$ K. A Si-low region exists near the melt-crystal interface due to the absorption of Si into crystal at all aspect ratios. However, due to the change in flow pattern the constant concentration lines are highly distorted at $A_r = 0.25$.

The time-averaged concentration distribution at the plane of the growth interface are displayed in Fig. 15 for three different aspect ratios for $\Delta T = 12.5$ K. The outer circle corresponds to crystal diameter. Owing to the small vortices nested under the crystal-melt interface, shown in Fig. 13, the concentration distribution consists of distorted 8 small rolls and a main roll. Projection of flow lines on a horizontal plane close to the crystal-melt interface (not shown) reveals the formation of vortices under the crystal similar to that shown in Fig. 6. However, the flow patterns are somewhat distorted due to loss of periodicity. At lower A_r, as the main vortex is closely pressed under the crystal-melt interface, more uniform concentration distribution is observed in the vicinity of the crystal. At $A_r = 0.25$, time averaged concentration distribution is almost concentric.

The circumferentially- and time-averaged variation of the Si concentration along the growth interface for $\Delta T = 12.5$ K for different aspect ratios is displayed in the radial direction at $\theta = 0$ in Fig. 16. The concentration is uniform and maximum at the free surface of the melt at all aspect ratios, due to the strong Marangoni convection induced by the surface tension effect which transports Si-rich mixture along the free surface to the crystal-melt interface. For all aspect ratios the concentration distribution at the crystal-melt interface resembles the "W" shape profile discussed earlier. A smaller aspect ratio will result higher melt velocities near the surface as shown in Fig. 12 due to increased surface tension effects. Higher fluid velocities under the crystal-melt interface will result in lower concentration differences (between maximum and minimum values) at the interface, the mechanism of which is described in discussions related with Fig. 8. As a result, the decrease in radial segregation (lower concentration differences at the crystal-melt

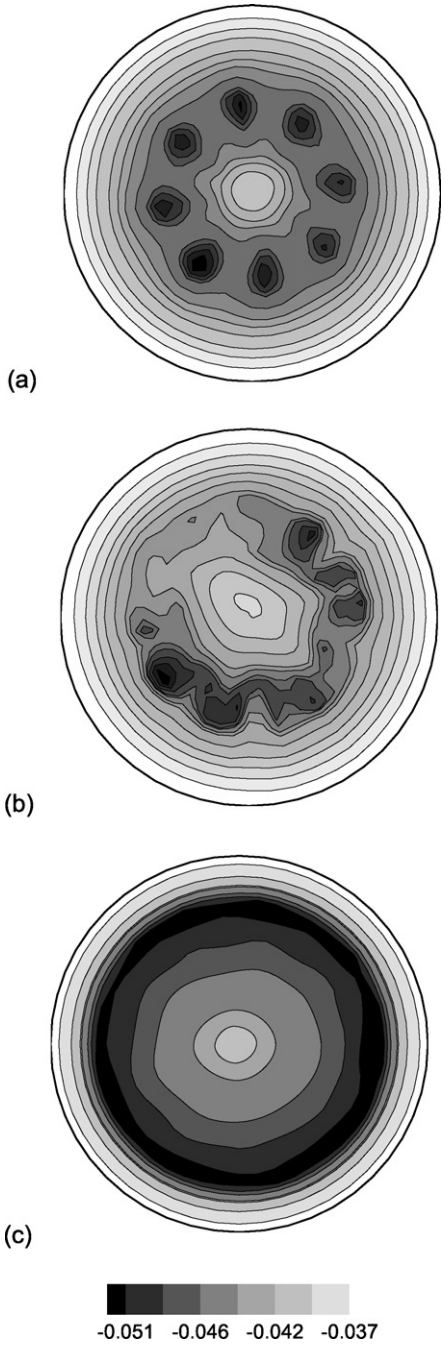

Fig. 15. Time-averaged concentration distribution at the plane of the growth interface for $\Delta T = 12.5$ K, (a) $A_r = 1.0$, (b) $A_r = 0.5$, (c) $A_r = 0.25$.

interface) at smaller aspect ratios seems logical. On the other hand, the decrease in Si concentration with lower aspect ratios is related with the decrease in volume of the melt with lower aspect ratios. With the assumption of constant growth rate, the decrease of mass of Si in the melt due to Si flow out at the crystal-melt interface is same for all aspect ratios, since same simulation time is used for all cases. However, decrease in Si concentration will be higher for lower aspect ratios since total mass of melt is smaller for lower aspect ratios, and that change in Si concentration is proportional to change in mass of Si divided by the total mass.

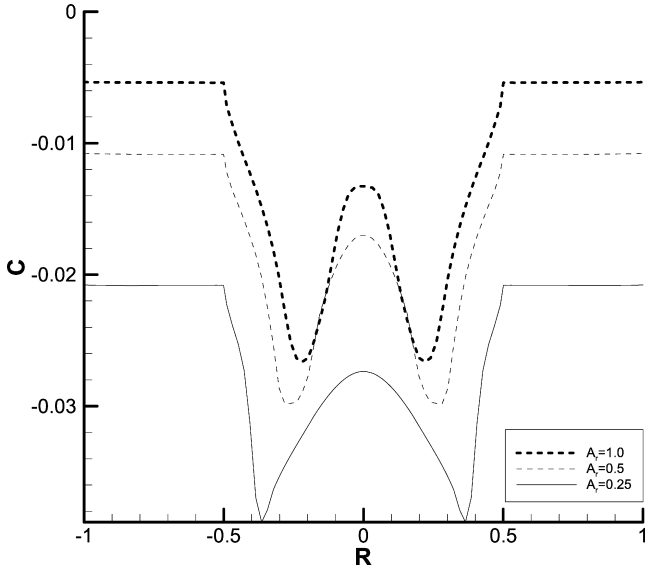

Fig. 16. Radial distribution of the circumferentially- and time-averaged Si concentration at the plane of the growth interface for different aspect ratios for $\Delta T = 12.5$ K.

In addition, it is found that the maximum Si concentration difference at the crystal-melt interface is smaller for lower aspect ratios due to higher melt velocities, which leads to better mixing in the vicinity of the crystal-melt interface. The behaviour of the oscillations is chaotic for all cases. However, it is observed that the frequency of the fluctuations increases as A_r decreases. Also, the amplitude of the fluctuations is lower at $A_r = 0.25$, which may be related with variations in flow pattern, that also affect concentration distribution. This variation may be attributed to overshadowed influence of the side walls by direct interactions between the bottom of the crucible, the crystal and the free surface of the melt and so the increased contribution of the Marangoni convection.

4. Conclusions

A series of unsteady 3-D numerical simulations were conducted to examine influence of melt flow on the distribution of Si at the growth interface of Ge_xSi_{1-x} single crystals by considering the buoyancy, thermal and solutal Marangoni convections. It was observed that the concentration distribution is significantly affected by the flow field. It was found that thermocapillary convection driven by the temperature difference at the surface prevents the development of the free surface concentration gradient necessary to drive solutocapillary convection.

The Si concentration radial distribution attains a “W” shape profile at the crystal-melt interface due to the counter rotating vortices formed below the crystal. It was found that radial homogeneity of the Si concentration in the interface improves at higher temperature differences due to higher flow velocities that lead to better mixing at the vicinity of the interface. As dopants in the melt has less time to be absorbed into the crystal at higher flow velocities at the vicinity of the interface, the difference between the maximum and minimum concentrations at the crystal-melt interface is smaller at higher temperature

differences. However, as the amplitude of the maximum concentration difference increases and exhibits a chaotic behaviour at higher temperature differences, which may lead striations, the dopant uniformity is not axisymmetric.

The effect of Marangoni convection is also examined and it is found that when Marangoni effect is absent, the flow intensity on the free surface of the melt decreases that leads increase in non-uniformity of dopant distribution at the crystal-melt interface.

When the melt depth in the crucible decreases, the flow structure changes influencing the Si concentration distribution at the growth interface. As the aspect ratio of the melt in the crucible decreases the radial segregation of Si at the crystal-melt interface improves due to higher velocities in the vicinity of the interface for moderate aspect ratio. However, it was found that the flow pattern changes at lower aspect ratios, which leads more uniform distribution of Si at the crystal-melt interface.

References

[1] Z. Galazka, H. Wilke, Influence of the Marangoni convection on the flow pattern in the melt during growth of $Y_3Al_5O_{12}$ single crystals by the Czochralski method, J. Crystal Growth 216 (2000) 389–398.

[2] Y.R. Li, L. Peng, Y. Akiyama, N. Imaishi, Three-dimensional numerical simulation of thermocapillary flow of moderate Prandtl number fluid in an annular pool, J. Crystal Growth 259 (2003) 374–387.

[3] Y.R. Li, N. Imaishi, P. Lan, S.Y. Wu, T. Hibiya, Thermocapillary flow in a shallow molten silicon pool with Czochralski configuration, J. Crystal Growth 266 (2004) 88–95.

[4] D. Schwabe, Buoyant-thermocapillary and pure thermocapillary convective instabilities in Czochralski systems, J. Crystal Growth 237–239 (2002) 1849–1853.

[5] V. Kumar, G. Biswas, G. Brenner, F. Durst, Effect of thermocapillary convection in an industrial Czochralski crucible: numerical simulation, Int. J. Heat Mass Transfer 46 (2003) 1641–1652.

[6] V. Kumar, B. Basu, S. Enger, G. Brenner, F. Durst, Role of Marangoni convection in Si-Czochralski melts—Part II: 3D predictions with crystal rotation, J. Crystal Growth 255 (2003) 27–39.

[7] Z. Zeng, J. Chen, H. Mizuseki, T. Fukuda, Y. Kawazoe, Three-dimensional unsteady convection in $LiCaAlF_6$-Czochralski growth, J. Crystal Growth 266 (2004) 81–87.

[8] A. Matsui, I. Yonenaga, K. Sumino, Czochralski growth of bulk crystals of $Ge_{1-x}Si_x$ alloys, J. Crystal Growth 183 (1998) 109–116.

[9] I. Yonenaga, Y. Murakami, Segregation during the seeding process in the Czochralski growth of GeSi alloys, J. Crystal Growth 191 (1998) 399–404.

[10] I. Yonenaga, Czochralski growth of GeSi bulk alloy crystals, J. Crystal Growth 198/199 (1999) 404–408.

[11] X. Niu, W. Zhang, G. Lu, Z. Jiang, Distribution of Ge in high concentration Ge- doped Czochralski-Si crystal, J. Crystal Growth 267 (2004) 424–428.

[12] Q. Xiao, Numerical simulations of transport processes during Czochralski growth of semiconductor compounds, J. Crystal Growth 174 (1997) 7.

[13] J.H. Wang, D.H. Kim, H.D. Yoo, Two-dimensional analysis of axial segregation in batchwise and continuous Czochralski process, J. Crystal Growth 198/199 (1999) 120.

[14] J.L. Morton, N. Ma, F.D. Bliss, G.G. Bryant, Dopant segregation during liquid-encapsulated Czochralski crystal growth in a steady axial magnetic field, J. Crystal Growth 242 (2002) 471–485.

[15] S. Enger, O. Gräbner, G. Müller, M. Breuer, F. Durst, Comparison of measurements and numerical simulations of melt convection in Czochralski crystal growth of silicon, J. Crystal Growth 230 (2001) 135–142.

[16] O.V. Smirnova, V.V. Kalaev, Y.N. Makarov, N.V. Abrosimov, H. Rieman, Simulation of heat transfer and melt flow in Czochralski growth of $Si_{1-x}Ge_x$ crystals, J. Crystal Growth 266 (2004) 74–80.

[17] J.P. Van Doormaal, G.D. Raithby, Enhancements of the simple method for predicting incompressible fluid flows, J. Numer. Heat Transfer 7 (1984) 147–163.

[18] B.P. Leonard, A stable and accurate convective modeling procedure based on quadratic upstream interpolation, J. Comput. Meth. Appl. Mech. Engrg. 19 (1979) 59–98.

[19] H.L. Stone, Iterative solution of implicit approximations of multi-dimensional partial differential equations, SIAM J. Numer. Anal. 5 (1968) 530–558.

[20] W. Hackbush, Iterative Solution of Large Sparse Systems, Springer, Berlin, 1994.

[21] H.A. Van Der Vorst, BiCGSTAB: A fast and smoothly converging variant of Bi-CG for the solution of non-symmetric linear systems, SIAM J. Sci. Statist. Comput. 13 (1992) 631–644.

[22] H. Ozoe, K. Toh, A technique to circumvent a singularity at a radial center with application for a three-dimensional cylindrical system, J. Numer. Heat Transfer 33 (1998) 355–365.

[23] S. Yesilyurt, L. Vujisic, S. Motakef, F.R. Szofran, M.P. Volz, A numerical investigation of the effect of thermoelectromagnetic convection (TEMC) on the Bridgman growth of $Ge_{1-x}Si_x$, J. Crystal Growth 207 (1999) 278–291.

[24] T.A. Campbell, M. Schweizer, P. Dold, A. Cröll, J.K.V. Benz, Float zone growth and characterization of $Ge_{1-x}Si_x$ ($x \leqslant 10$ at%) single crystals, J. Crystal Growth 226 (2001) 231–239.

[25] M.V. Farrell, N. Ma, Macrosegregation during alloyed semiconductor crystal growth in strong axial and transverse magnetic fields, Int. J. Heat Mass Transfer 47 (2004) 3047–3055.

[26] P. Dold, N. Kaiser, K.W. Benz, A. Cröll, F.R. Szofran, S. Cobb, M. Volz, M. Schweizer, in: Proceedings of 51th International Astronautical Congress, Rio De Janerio, Brasil, 2000, pp. 1–12.

[27] I. Yonenaga, M. Sakurai, M. Nonaka, T. Ayuzawa, M.H.F. Sluiter, Y. Kawazoe, Local strain relaxation in Czochralski-grown GeSi bulk alloys, Physica B 340–342 (2003) 854–857.

[28] R.W. Olesinski, G.J. Abbaschian, The Ge–Si system, Bull. Alloy Phase Diagrams 5 (1984) 180–183.

[29] B.C. Sim, A. Zebib, D. Schwabe, Oscillatory thermocapillary convection in open cylindrical annuli. Part 2. Simulations, J. Fluid Mech. 491 (2003) 259–274.

[30] H. Nakanishi, M. Watanabe, K. Terashime, Dependence of Si melt flow in a crucible on surface tension variation in the Czochralski process, J. Crystal Growth 236 (2002) 523–528.

[31] A.Y. Gelfgat, Different modes of Rayleigh–Benard instabilities in two and three dimensional rectangular enclosures, J. Comput. Phys. 156 (1999) 300–324.

[32] J. Xu, A. Zebib, Oscillatory two- and three-dimensional thermocapillary convection, J. Fluid Mech. 364 (1998) 187–209.